

A New Threshold Relative Radiometric Correction Algorithm (TRRCA) of Multiband Satellite Data

Antonio Novelli¹(✉), Manuel A. Aguilar², and Eufemia Tarantino¹

¹ Politecnico di Bari, via Orabona 7, 70125 Bari, Italy
{antonio.novelli,eufemia.tarantino}@poliba.it

² Department of Engineering, University of Almería, 04120 Almería, Spain
maguilar@ual.es

Abstract. It is well known that remote sensed scenes could be affected by many factors and, for optimum change detection, these unwanted effects must be removed. In this study a new algorithm is proposed for PIF (Pseudo Invariant Features) extraction and relative radiometric normalization. The new algorithm can be labeled as a supervised one and combines three methods for the detection of PIFs: Moment distance index (MDI), Normalized Difference Vegetation Index (NDVI) masks morphological erosion and dilate operators. In order to prove its effectiveness, the algorithm was tested by using Landsat 8 scenes of the “Mar de Plástico” landscape of the Andalusian Almería. Many tests were performed in order to provide a set of valid input parameters for the chosen environments. Lastly, the results were statistically assessed with parametric and non-parametric tests showing very good and stable results in the four different study areas.

Keywords: Relative radiometric normalization · PIF · Multispectral imagery · Landsat 8 · Change detection

1 Introduction

In the last decades, satellite image analysis has provided invaluable data for environment monitoring and change detection (CD) analysis [1–3]. However, remote sensing observations are instantaneous and affected by many factors (e.g. such as atmospheric conditions) [4]. These unwanted effects must be removed for radiometric consistency among temporal images. To detect measurable landscape changes, it is necessary to carry out a radiometric correction. Two approaches to radiometric correction are possible: absolute and relative radiometric normalization (RRN) [5]. In absolute radiometric correction, atmospheric radiative-transfer codes (e.g. 6Sv, MODTRAN) are used to obtain the reflectance at the Earth’s surface from the measured spectral radiances. These techniques depend on in situ data and sensor. Consequently, for most historically remote scenes, absolute surface reflectance retrieval may not always be practical [4].

An alternative to absolute radiometric correction is relative correction, which is commonly used in one of two ways; adjusting bands of data within a single image and normalizing bands in images of multiple dates relative to a Reference (R) image [6]. Relative methods are applied at least on two scenes, the reference and one or more target (T) (e.g. the Dark-object subtraction (DOS) [7] and the histogram matching (HM) [8]). Many researchers opt for a linear radiometric normalization method for multi temporal analysis (e.g. [9]). The common form for linear radiometric image normalization is Eq. 1

$$Y_k^N = g_k \times X_k + o_k \quad (1)$$

Here X_k is the reflectance from the k^{th} band of the target scene X , Y_k^N is the normalized reflectance of the k^{th} band of the reference scene Y , g_k and o_k are respectively the evaluated gain and offset implemented for the k^{th} band of the target scene. Several methods have been proposed for the radiometric normalization with linear regression of multitemporal images (e.g. [9, 10]). The first attempts were based on simple regression considering all pixels of multitemporal images [6, 11]. Subsequently, normalization was performed considering landscape elements with reflectance values that are nearly constant over time. These areas belong to the so called pseudo-invariant features (PIF) [12, 13].

This paper shows a new PIF selecting algorithm combining Moment Distance Index (MDI) [14, 15] thresholding, Normalized Difference Vegetation Index (NDVI) masks and morphological erosion and dilation operators. The proposed method was called Threshold Relative Radiometric Correction Algorithm (TRRCA) and was designed in a Python 2.7 environment. The algorithm was tested in the Mar de Plástico landscape of Almería (Spain) in which were defined a set of optimal input parameters to statistically assess the TRRCA results. To the author’s knowledge this is the first method that takes into account both the MDI and morphological operators (typically implemented in image filtering problems, e.g. [16, 17]).

2 Study Area and Data

The test area falls in the so-called “Sea of Plastic” (Mar de Plástico in Spanish), in the province of Almería (Southern Spain Fig. 1). The main economic activity is agriculture under plastic covered greenhouses [15] that implements different typologies of plastic materials to cover greenhouse structures. The climate is semi-arid and plastic covered greenhouses are coupled with the use of groundwater [18] as often happens in other semi-arid Mediterranean regions

Table 1. Reference (R) and Target (T) scenes used in this study.

Acquisition date	Scene ID	Subset
13 July 2014	LC82000342014194LGN00	R-S
30 June 2016	LC82000342015181LGN00	T-S

(e.g. [19, 20]). The “Sea of Plastic” test area was chosen to test the TRRCA with homogenous artificial areas (high number of common artificial reflectors) with two Landsat 8 scenes (Table 1).

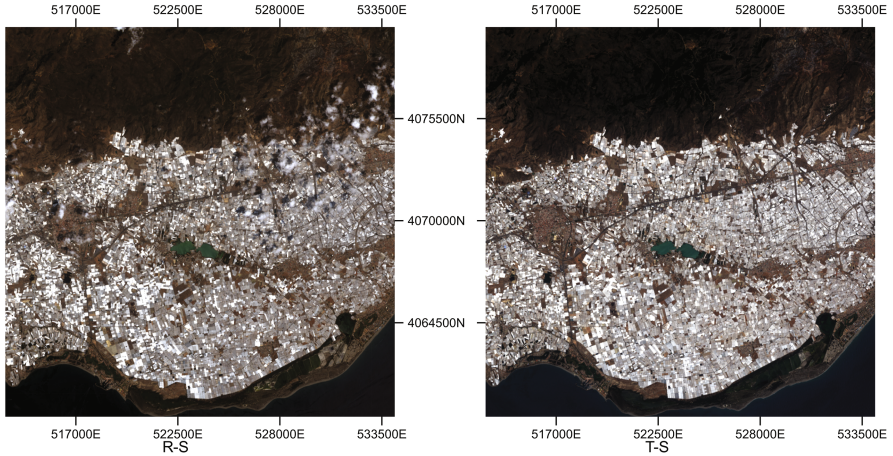


Fig. 1. Reference-Spanish (R-S) and Target-Spanish (T-S) scenes used in this study. Coordinate System UTM WGS 84 zone 30N.

Landsat 8 satellite takes images covering the entire Earth every 16 days and carries a two-sensor payload, the Operational Land Imager (OLI) and the Thermal Infrared Sensor (TIRS). The OLI and TIRS spectral bands remain broadly comparable to the Landsat 7 Enhanced Thematic Mapper plus (ETM+) bands. Further details on OLI and TIRS band specification (e.g. data format, level of processing, etc.) can be found in [21]. The OLI digital numbers of the eight Landsat 8 images were linearly converted to sensor Top of Atmosphere (TOA) reflectance and then corrected for the sun angle using gains, offsets and local sun elevation values stored in each scene metadata (as defined in the Landsat 8 (L8) Data User Handbook). The integrity of the subsets extracted from the two scenes was checked through the Landsat 8 Quality Assessment (QA) Band and the L-LDOPE Toolbelt, a no-cost tool available from the USGS Landsat-8 website [22].

3 Method

The PIF selection algorithm combines the extraction of dark (local minimum) and bright (local maximum) targets through morphological operators (M_{morph}), NDVI masks (M_{NDVI}) and MDI measures (M_{MDI}). Only the pixels positive to all the imposed conditions are selected as PIF (Eq. 2). The method was not designed to deal with the panchromatic, the cirrus and the two TIRS bands.

$$PIF = M_{morph} \cap M_{NDVI} \cap M_{MDI} \quad (2)$$

According to [23], if the selected scenes own common local maximum and minimum values within specific bands, then the considered locations can be considered as candidate PIF. In this paper, the blue band was used to locate local minimum (often corresponding to water bodies) while bare soil or man-made objects were located through the red band. They were respectively found by using the morphological erosion and dilation. The erosion (dilation) of a digital greyscale image A by a flat structuring element S (at any location) is defined as the minimum (maximum) value of the image within the region coincident with S [8, 24]. In the subsequent equations, S is defined by a square $n \times n$ matrix with all elements equal to 1. The influence of the structuring element size over the achieved PIF extraction was tested considering seven n in the closed interval [3; 15] with $n \in 2\mathbb{N} + 1$. Bright and dark PIF were found by means of Eqs. 3 and 4, considering the morphological dilation (\oplus for M_{max}) and erosion (\ominus for M_{min}) common outputs for the considered bands.

$$M_{max} = [(Band_4^R \oplus S) \cap Band_4^R] \cap [(Band_4^T \oplus S) \cap Band_4^T] \quad (3)$$

$$M_{min} = [(Band_2^R \ominus S) \cap Band_2^R] \cap [(Band_2^T \ominus S) \cap Band_2^T] \quad (4)$$

$$M_{morph} = M_{max} \cup M_{min} \quad (5)$$

Pixels selected through Eqs. 3 and 4 were used to create the M_{morph} mask (Eq. 5). PIF selected through Eq. 5 could fall within vegetated areas. Moreover, they could not be invariant pixel for other bands. To increase the quality of the selected PIF, the TRRCA introduces a vegetation mask derived from the very well-known NDVI [25] computed from both R and T scenes. The selection of these areas was achieved fixing three NDVI thresholds ($NDVI_{max} > NDVI_{mid} > NDVI_{min}$) by creating a further NDVI mask with Eq. 6.

$$M_{NDVI} = \{[(NDVI_R < NDVI_{max}) \cap (NDVI_T < NDVI_{max})] \cap [(NDVI_R > NDVI_{mid}) \cap (NDVI_T > NDVI_{mid})]\} \cup [(NDVI_R < NDVI_{min}) \cap (NDVI_T < NDVI_{min})] \quad (6)$$

To test the influence of these thresholds the following interval of values were tested with a step of 0.05: $0.00 \leq NDVI_{max} < 0.26$; $-0.10 \leq NDVI_{mid} < 0.16$; $-0.60 \leq NDVI_{min} < -0.096$.

In addition to the aforementioned masks, the TRRCA takes advantage of the MDI. To the best knowledge of the authors, it is the first time that MDI is tested in RRN problems. The MDI is designed to describe the distribution of reflectance values associated with a pixel by calculating the moment distances among the bands (further details can be found in [14]): for this reason, its contribution was added in the proposed algorithm. Computationally, the MDI is calculated, for each pixel of the reference and target subset, from the difference (Eq. 7) of the moment distance (MD) between a right and a left pivot (λ_{RP} and λ_{LP} expressed in μm).

$$MDI = \sum_{i=\lambda_{LP}}^{\lambda_{RP}} \sqrt{[\rho^2 + (i - \lambda_{LP})^2]} - \sum_{i=\lambda_{RP}}^{\lambda_{LP}} \sqrt{[\rho^2 + (\lambda_{LP} - i)^2]} \quad (7)$$

Where ρ is the reflectance for the band centred on the i^{th} wavelength. Only the pixels in which the absolute value of the difference between the two MDI (Eq. 8) is less than a specific threshold (l) were considered as potentials PIF.

$$M_{MDI} = |MDI^R - MDI^T| < l \rightarrow MDI_{diff} < l \quad (8)$$

Several values of l within the semi-opened interval $[0.01; 0.31]$, with a step of 0.03, were tested. Considering the implemented values, a $MDI_{diff} = 0.30$ corresponds to 9 – 12% of difference between MDI^R and MDI^T .

Lastly, the radiometric normalization coefficients were evaluated for each band by means of the Orthogonal Distance Regression (ODR) algorithm implemented in the ODRPACK library (further details on the solution implemented can be found in [26]). The ODR algorithm outputs are the gains and the offsets for each band (as shown in Eq. 1), the root mean square error ($RMSE$), the correlation coefficient (r) and the coefficient of determination (R^2) between PIF belonging to the R and the T scenes. Almost twenty thousand combinations were performed considering the selected parameter S , l , $NDVI_{max}$, $NDVI_{mid}$, $NDVI_{min}$. Only tests characterized by an elevated number of retrieved PIF, with high R-T band by band ODR R^2 and low ODR $RMSE$ were selected as potentials High Quality PIF (HQ-PIF) extractions. Particularly, the above PIF extractions were considered HQ-PIF only if the two-sample t test (for equal sample means), the two-sample F test (for equal sample variances) and two-sample Wilcoxon rank sum test (for equal sample medians) between reference PIF and corrected target PIF were contemporary satisfied at 5% confidence level.

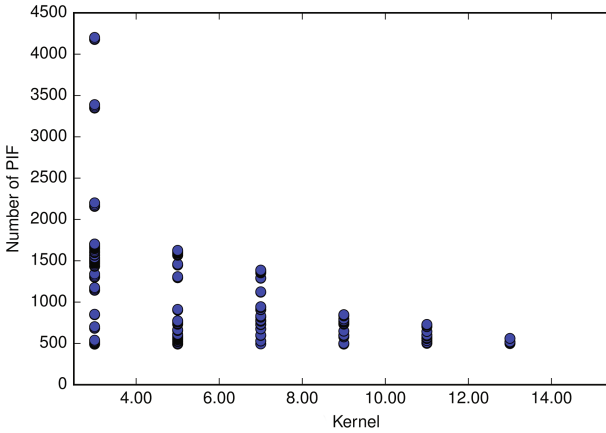
4 Results and Discussion

Table 2 summarizes the results for the tested parameters related to HQ-PIF extractions. The computations executed for the study area showed 1503 HQ-PIF extraction with a mean number of PIF equal to 984 pixels. This result shows the sensitivity of the proposed algorithm to the abundance of natural/artificial reflectors.

All the tested $NDVI_{mid}$ and $NDVI_{min}$ values are present in HQ-PIF extractions. $NDVI_{mid}$ and l are the parameters that exhibit the major variability. Probably, this occurs since the test area is less sensitive to these parameters. Indeed, the effect on NDVI is masked by the presence of plastic coverings above the vegetation. For the $NDVI_{max}$ the peak of frequency is equivalent to the maximum value tested. This shows that the M_{NDVI} performs as a coarse PIF filter for a subsequent and improved PIF selection through M_{MDI} and M_{morph} . The same occurs for the l parameter which great variability depicts the spectral difference form the R and the T scenes. Lastly, the tests demonstrated that lower kernels sizes (S) are coupled with a greater number of extracted PIF (Fig. 2).

Table 2. Statistical parameters of the of the implemented TRRCA parameters and of the number of HQ-PIF extractions..

	S	l	$NDVI_{max}$	$NDVI_{mid}$	$NDVI_{min}$	N_{pif}
Min	3	0.01	0.10	-0.10	-0.60	491
Max	13	0.28	0.25	0.15	-0.10	4203
Mode	5	0.04	0.25	0.10	-0.60	599
Median	7	0.10	0.20	0.10	-0.35	774
Dev. stand	3	0.08	0.04	0.07	0.16	532
Mean	7	0.11	0.21	0.08	-0.35	984

**Fig. 2.** Scatter plot Kernel - number of PIF.

This was also an expected result since morphological operators consider the local minimum and local maximum over the Kernel area. Because of this, the probability to find a corresponding singular value over the same Kernel areas is higher in smaller areas than in greater ones.

Since the proposed algorithm is dependent from user driven parameters the results showed in Table 2 have been used to select one single test combination. The combination was randomly extracted from the test parameters characterized by a high frequency of occurrence and removing the restriction adopted during the test phase to save computation time (i.e. the step). Table 3 shows the selected parameters and the related number of PIF.

Table 3. Implemented thresholds and kernel size.

S	l	$NDVI_{max}$	$NDVI_{mid}$	$NDVI_{min}$	N_{pif}
7	0.03	0.221	0.100	-0.503	893

Figure 3 compares the RGB visualizations of a magnified area of R and corrected T with overlapped TRRCA HQ-PIF. In the test area, the major part of the PIF falls within artificial pools, bare soil, built-up areas and highways. Although the large amount of plastic covered greenhouses, PIF do not fall within them. Indeed, greenhouses are generally covered by plastic sheets characterized by different spectral signatures over time. This is mainly due to their different spectral properties, thickness and local agricultural practices [27, 28].

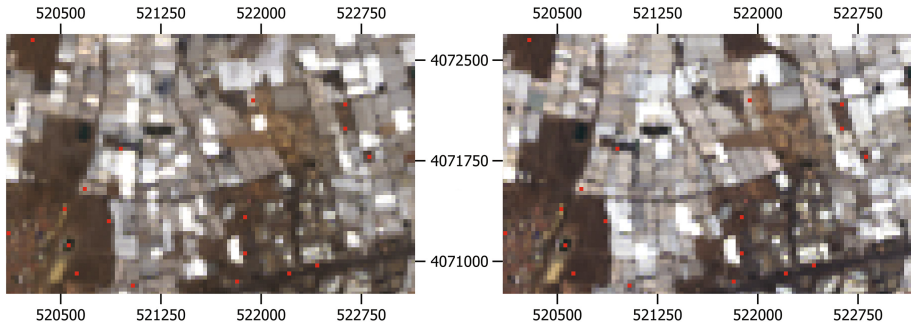


Fig. 3. Comparison of RGB visualizations of Reference (R) image (on the left) and corrected Target (T) image (on the right) with overlapped PIF: Coordinate System UTM WGS 84 zone 30N

Table 4 compares the achieved gains, offsets, correlation coefficient (r), $RMSE$, two-sample t test, two-sample F test and two-sample Wilcoxon rank sum test results achieved for the selected parameters before (Pre) and after (Post) the correction. The table shows that the TRRCA was able to find PIF with a strong linear agreement in each test area. For each computed gains the significance of the linear relationship was tested against the null hypothesis of absence of slope. All tests strongly rejected the null hypothesis. It is thus possible to conclude that the method produces a feasible linear regression model.

Considering the evaluated r and $RMSE$, Table 4 always shows high quality and stable results (small variance). After the application of the correction all the performed tests failed to reject the null hypothesis. Moreover, p-values indicate that all the null hypothesis would be accepted by using a level of confidence far beyond the default one. Considering each typology of test, this respectively indicates a strong statistical similarity between the variance, the means and medians of the reflectance values of test PIF extracted from the reference and corresponding normalized reflectance values of PIF extracted from the target. This was an expected result since the definition of HQ-PIF imposes the respect of all statistical tests. The effects of the corrections were bigger on the median of the distributions of the selected PIF. This is demonstrated by the pre/post Wilcoxon rank sum test.

Table 4. Evaluated band-by-band gain, offset, correlation r and RMSE; F p-value, t p-value, W p-value are p-values for the two sample F test, two sample t test and the Wilcoxon rank sum test. The result $h = 1$ indicates a rejection of the null hypothesis, and $h = 0$ indicates a failure to reject the null hypothesis at the 5% significance level.

Band	gain	offset	r	RMSE	F p		F h		t p		t h		W p		W h	
					Pre	Post										
1	1.076	-0.006	0.96	0.01	0.0	0.9	1	0	0.0	1.0	1	0	0.0	0.8	1	0
2	1.063	-0.006	0.97	0.01	0.1	1.0	0	0	0.0	1.0	1	0	0.0	0.7	1	0
3	1.081	-0.013	0.96	0.01	0.0	0.9	1	0	0.7	1.0	0	0	0.0	0.3	1	0
4	1.116	-0.023	0.96	0.01	0.0	0.9	1	0	0.8	1.0	0	0	0.0	0.4	1	0
5	1.190	-0.051	0.95	0.02	0.0	0.8	1	0	0.7	1.0	0	0	0.7	0.5	0	0
6	1.272	-0.066	0.96	0.02	0.0	0.8	1	0	0.0	1.0	1	0	0.0	0.7	1	0
7	1.255	-0.045	0.96	0.02	0.0	0.8	1	0	0.0	1.0	1	0	0.0	0.5	1	0

5 Conclusions

This paper shows a new PIF selecting algorithm combining spectral momentum measures, NDVI masks and extraction of local maximum and minimum through morphological operators. The method was tested with Landsat-8 images but its design is suitable for other passive sensors with a similar spectral resolution (e.g. Sentinel-2). Due to its dependence by user driven thresholds, many combinations were tested in the selected test area characterized by the presence of an extreme anthropic impact. All the tests performed were driven to obtain the distribution of thresholds able to perform a good relative radiometric normalization. To show the capabilities of the method was randomly selected a set of parameters. In this case, the proposed algorithm recognized a great number of PIF and performed a correction on the selected PIF able to eliminate statistical differences between reference PIF and corrected target PIF. The results confirm the effectiveness of the method as new relative radiometric normalization technique and as a valid alternative to established methods from scientific literature. Future development will be focused on the improvement of the quality of selected PIF, on the analysis of a greater spectral range and in an improved reduction of user driven parameter.

Acknowledgement. This work was supported by the Spanish Ministry of Economy and Competitiveness (Spain) and the European Union FEDER funds (Grant Reference AGL2014-56017-R). It takes part of the general research lines promoted by the Agrifood Campus of International Excellence ceiA3.

References

1. Janzen, D.T., Fredeen, A.L., Wheate, R.D.: Radiometric correction techniques and accuracy assessment for landsat TM data in remote forested regions. *Can. J. Remote Sens.* **32**(5), 330–340 (2006)
2. Novelli, A., Caradonna, G., Tarantino, E.: Evaluation of relative radiometric correction techniques on landsat 8 OLI sensor data. In: Fourth International Conference on Remote Sensing and Geoinformation of the Environment, International Society for Optics and Photonics 968808 (2016)
3. Tarantino, E., Novelli, A., Aquilino, M., Figorito, B., Fratino, U.: Comparing the MLC and JavaNNS approaches in classifying multi-temporal LANDSAT satellite imagery over an ephemeral river area. *Int. J. Agric. Environ. Inf. Syst. (IJAEIS)* **6**(4), 83–102 (2015)
4. Du, Y., Teillet, P.M., Cihlar, J.: Radiometric normalization of multitemporal high-resolution satellite images with quality control for land cover change detection. *Remote Sens. Environ.* **82**(1), 123–134 (2002)
5. Yang, X., Lo, C., et al.: Relative radiometric normalization performance for change detection from multi-date satellite images. *Photogram. Eng. Remote Sens.* **66**(8), 967–980 (2000)
6. Jensen, J.: Image preprocessing: Radiometric and geometric correction. In: *Introductory Digital Image Processing*, 30p (1996). Chapter 6
7. Mandanici, E., Franci, F., Bitelli, G., Agapiou, A., Alexakis, D., Hadjimitsis, D.: Comparison between empirical and physically based models of atmospheric correction. In: Third International Conference on Remote Sensing and Geoinformation of the Environment, International Society for Optics and Photonics 95350E (2015)
8. Gonzalez, R.C., Woods, R.E., Eddins, S.: Morphological image processing. *Digit. Image Process.* **3**, 627–688 (2008)
9. Canty, M.J., Nielsen, A.A.: Automatic radiometric normalization of multitemporal satellite imagery with the iteratively re-weighted mad transformation. *Remote Sens. Environ.* **112**(3), 1025–1036 (2008)
10. de Carvalho, O.A., Guimarães, R.F., Silva, N.C., Gillespie, A.R., Gomes, R.A.T., Silva, C.R., de Carvalho, A.P.F.: Radiometric normalization of temporal images combining automatic detection of pseudo-invariant features from the distance and similarity spectral measures, density scatterplot analysis, and robust regression. *Remote Sens.* **5**(6), 2763–2794 (2013)
11. Tokola, T., Löfman, S., Erkkilä, A.: Relative calibration of multitemporal LANDSAT data for forest cover change detection. *Remote Sens. Environ.* **68**(1), 1–11 (1999)
12. Caselles, V., Garcia, M.L.: An alternative simple approach to estimate atmospheric correction in multitemporal studies. *Int. J. Remote Sens.* **10**(6), 1127–1134 (1989)
13. Schott, J.R., Salvaggio, C., Volchok, W.J.: Radiometric scene normalization using pseudoinvariant features. *Remote Sens. Environ.* **26**(1) 1–14, IN1, 15–16 (1988)
14. Salas, E.A.L., Boykin, K.G., Valdez, R.: Multispectral and texture feature application in image-object analysis of summer vegetation in eastern tajikistan pamirs. *Remote Sens.* **8**(1), 78 (2016)
15. Aguilar, M.A., Nemmaoui, A., Novelli, A., Aguilar, F.J., Lorca, A.G.: Object-based greenhouse mapping using very high resolution satellite data and landsat 8 time series. *Remote Sens.* **8**(6), 513 (2016)
16. Tarantino, E., Figorito, B.: Steerable filtering in interactive tracing of archaeological linear features using digital true colour aerial images. *Int. J. Digit. Earth* **7**(11), 870–880 (2014)

17. Tarantino, E., Figorito, B.: Extracting buildings from true color stereo aerial images using a decision making strategy. *Remote Sens.* **3**(8), 1553–1567 (2011)
18. Van Cauwenbergh, N., Pinte, D., Tilmant, A., Frances, I., Pulido-Bosch, A., Vanclooster, M.: Multi-objective, multiple participant decision support for water management in the andarax catchment, almeria. *Environ. Geol.* **54**(3), 479–489 (2008)
19. Giordano, R., Milella, P., Portoghese, I., Vurro, M., Apollonio, C., D’Agostino, D., Lamaddalena, N., Scardigno, A., Piccinni, A.: An innovative monitoring system for sustainable management of groundwater resources: Objectives, stakeholder acceptability and implementation strategy. In: 2010 IEEE Workshop on Environmental Energy and Structural Monitoring Systems (EESMS), pp. 32–37. IEEE (2010)
20. Giordano, R., D’Agostino, D., Apollonio, C., Scardigno, A., Pagano, A., Portoghese, I., Lamaddalena, N., Piccinni, A.F., Vurro, M.: Evaluating acceptability of groundwater protection measures under different agricultural policies. *Agric. Water Manage.* **147**, 54–66 (2015)
21. Roy, D.P., Wulder, M., Loveland, T., Woodcock, C., Allen, R., Anderson, M., Helder, D., Irons, J., Johnson, D., Kennedy, R., et al.: Landsat-8: Science and product vision for terrestrial global change research. *Remote Sens. Environ.* **145**, 154–172 (2014)
22. Roy, D.P., Borak, J.S., Devadiga, S., Wolfe, R.E., Zheng, M., Descloitres, J.: The modis land product quality assessment approach. *Remote Sens. Environ.* **83**(1), 62–76 (2002)
23. Hall, F.G., Strebel, D.E., Nickeson, J.E., Goetz, S.J.: Radiometric rectification: Toward a common radiometric response among multirate, multisensor images. *Remote Sens. Environ.* **35**(1), 11–27 (1991)
24. Soille, P.: *Morphological Image Analysis: Principles and Applications*. Springer, Heidelberg (2013)
25. Tucker, C.J.: Red and photographic infrared linear combinations for monitoring vegetation. *Remote Sens. Environ.* **8**(2), 127–150 (1979)
26. Boggs, P.T., Byrd, R.H., Schnabel, R.B.: A stable and efficient algorithm for non-linear orthogonal distance regression. *SIAM J. Sci. Stat. Comput.* **8**(6), 1052–1078 (1987)
27. Novelli, A., Aguilar, M.A., Nemmaoui, A., Aguilar, F.J., Tarantino, E.: Performance evaluation of object based greenhouse detection from sentinel-2 MSI and landsat 8 OLI data: A case study from Almería (Spain). *Int. J. Appl. Earth Obs. Geoinformation* **52**, 403–411 (2016)
28. Novelli, A., Tarantino, E.: Combining ad hoc spectral indices based on LANDSAT-8 OLI/TIRS sensor data for the detection of plastic cover vineyard. *Remote Sens. Lett.* **6**(12), 933–941 (2015)